AcroMELD: Recovering Interactive PDF Forms with Structure-Aware Graph Set Transformers

Samuel Abramov
Accessful GmbH
samuel@accessful.de
ORCID: 0009-0007-4511-0739

3 August 2026

arXiv:2608.22338v1 [cs.CV] 23 Aug 2026

Abstract

Interactive PDF form fields are often absent from documents that visually resemble forms, leaving users unable to enter data without printing or external editing tools. Detecting the missing widgets is difficult because a field may be indicated by several overlapping cues, born-digital PDFs expose useful but incomplete drawing structure, and dense pages can contain hundreds of fields. We introduce AcroMELD (*AcroForm Multi-source Evidence Linking Decoder*), a 39.4M-parameter detector that combines a high-resolution visual transformer with label-free PDF primitives. Its 896-query set comprises 384 visual proposals, 384 structure-seeded proposals, and 128 learned recovery queries. Four graph-set layers exchange information over geometry-biased sparse neighborhoods and cross-attend to PDF structure. A learned same-field relation links co-referent candidates, while a localization-quality head is trained on the containment-aware overlap used by the downstream recovery decision. We define a hash-bound evaluation protocol with disjoint development, calibration, internal-test, and quarantined external-holdout roles. The sealed, single-seed candidate reaches native containment micro-F_1 0.9344 on the internal test and 0.8477 on the one-shot external holdout (95% PDF-cluster bootstrap interval 0.8339–0.8605). This passes the registered historical FFGBT-v8 reference by 0.0186 absolute F_1. Under the stricter external adapter, however, performance is 0.7786 IoU-0.5 F_1 and 0.2900 COCO mAP, below a locally evaluated CommonForms-L reference; the signature class receives no prediction at the selected threshold. Thus the result supports the registered operational gate while exposing substantial domain and rare-class limitations.

1 Introduction

A PDF can look like a form without containing interactive form controls. This occurs in scanned paperwork and in born-digital documents whose lines and boxes were authored only as page graphics. The visual appearance is preserved, but the AcroForm widgets needed for direct data entry are absent. Recovering candidate widget geometries is therefore a useful first step toward making such documents fillable. It is also only one step. Accessible PDF forms require keyboard-operable controls, programmatically exposed names, roles, states, and values, a logical tab and reading order, and appropriate instructions and error feedback [1–5]. We deliberately study the narrower, measurable problem of localizing and classifying missing field controls.

Recent work casts form-field detection as object detection and demonstrates the importance of high-resolution page images [6]. A raster, however, discards information that already exists in a born-digital PDF. Text runs, line segments, rectangles, paths, and images carry spatial evidence about candidate fields. That evidence is neither a ground-truth annotation nor universally available: a rectangle may be decorative, a text line may be underlined for emphasis, and a scanned document may expose no useful primitives. Consequently, PDF structure should complement rather than replace visual evidence.

Combining these sources introduces a set-prediction problem that is easy to overlook. The same field can produce a visual proposal, one or more structure-derived proposals, and a learned recovery proposal. Standard one-to-one assignment discourages duplicate final predictions [7], but it does not by itself provide an explicit inference-time statement that two source-specific candidates refer to the same field. Dense pages amplify the problem: our sealed corpus contains a page with 849 valid widgets, well beyond a conventional Top-300 detection cap. Aggressive non-maximum suppression is also unsafe because neighboring form controls may legitimately touch or nest.

We propose AcroMELD, an AcroForm Multi-source Evidence Linking Decoder. A compact visual transformer produces 384 proposals, a label-free PDF encoder seeds another 384, and 128 learned queries recover fields missed by both sources. The resulting 896-node set is refined by four graph layers with sparse, geometry-biased self-attention and full cross-attention to the PDF primitives. Each node predicts a field class, a box, a containment-aligned

localization quality, and a normalized embedding whose pairwise similarity estimates whether candidates describe the same field. Decoding greedily retains representatives and suppresses spatially eligible candidates inferred to co-refer, without imposing a class-specific duplicate rule.

Our evaluation design treats result provenance as part of the method. Document groups are split into five non-overlapping roles; class thresholds and representative-selection parameters were fit only on calibration data; the candidate was cryptographically frozen before internal test inference; and a quarantined external corpus was evaluated once after the completed training lineage validated. We report both the operational containment criterion and strict COCO-style localization metrics [8]. Keeping them separate prevents a box that merely lies inside a target from being mistaken for precise localization.

This work makes four contributions:

- A multi-source query formulation that preserves visual, PDF-structural, and unconstrained recovery evidence in one exclusive set whose capacity is derived from measured page density.
- A geometry-aware graph-set decoder with an explicitly supervised same-field relation, allowing candidates to exchange context and be consolidated at inference.
- A localization-confidence objective aligned with the containment-aware recovery decision, while retaining L1 and generalized-IoU losses and strict COCO evaluation as precision safeguards [9, 10].
- A leakage-resistant experimental protocol that binds data, code, configuration, checkpoints, operating points, and final reports by content hashes.

The registered run completed 33 epochs, froze one candidate and operating point, evaluated internal test only after that freeze, and then executed the one-shot external gate. Its calibrated and fixed-threshold external results differ materially. With only this training trajectory, the evidence concerns the complete frozen system rather than the effect of any one component.

2 Related Work

2.1 Form fields and document layout

CommonForms formalized field detection as three-class object detection over text inputs, choice controls, and signature fields, and introduced the high-resolution FFDNet family [6]. This differs from form understanding datasets such as FUNSD, where the objective is to connect and semantically interpret text entities [11]. Large layout corpora including PubLayNet and DocLayNet instead annotate regions such as paragraphs, tables, figures, and headings [12, 13]. These tasks provide valuable document representations, but their semantic regions do not directly specify interactive widget boxes. AcroMELD follows the CommonForms field taxonomy while incorporating low-level PDF primitives that are normally discarded during rasterization.

2.2 Multimodal document models

LayoutLM and later variants jointly encode text, geometry, and image information for document understanding [14, 15]. DocFormer similarly learns cross-modal interactions between visual and textual features [16]. Their usual output is a token-, region-, or document-level semantic prediction. Our problem instead requires a high-cardinality, variable-size set of precise boxes and must continue to operate when text or PDF structure is absent. We therefore use a small structure encoder as conditional geometric evidence rather than a document-language backbone.

2.3 Transformer detection and relational sets

DETR frames object detection as direct set prediction with bipartite matching [7]; Deformable DETR reduces attention cost using sparse sampling [17]. Our visual branch derives from ECDet-L in EdgeCrafter, a compact-ViT dense-prediction family [18]. We retain its COCO-pretrained multiscale visual proposal generator, then change the downstream problem from a single proposal source to a heterogeneous query set.

The Set Transformer established attention-based permutation-invariant processing of sets [19]. Relation Networks showed that geometry-aware interactions can improve recognition and duplicate removal in object detection [20]. Our graph-set layers draw on both ideas but use the current box hypotheses to define a 32-neighbor spatial graph. Unlike generic NMS, a separately supervised link embedding represents same-field co-reference across query origins and participates directly in representative selection.

2.4 Localization confidence

Classification probability alone need not rank the best localized box. IoU-Net addressed this misalignment by predicting localization confidence for ranking and suppression [9]. In form recovery, the operational criterion may accept either a close box or a geometrically contained one. We train quality against that declared criterion, but still optimize exact box fit and publish strict IoU metrics. This dual reporting is important because containment alone can overvalue an undersized prediction.

3 Problem Definition and Protocol

3.1 Field-recovery task

For a PDF page, the model receives a raster image I and an optional sequence of label-free structure tokens S. Each token represents a text word, line, rectangle, path, image, or the page itself. It contains a normalized box, a 32-dimensional primitive descriptor, at most 48 UTF-8 bytes, and an availability flag. Existing AcroForm widget annotations and field types are not exposed through S. If extraction fails or the page is scanned, S is a single unavailable page sentinel.

The target is an unordered set

$$\begin{aligned} &Y = \{(b_j, c_j)\}_{j=1}^{n}, \\ &c_j \in \{\textsc{Text}, \textsc{Choice}, \textsc{Signature}\}. \end{aligned} \tag{1}$$

where b_j is an axis-aligned widget box in page coordinates. We predict the geometry and coarse control type needed to instantiate candidate widgets. We do not predict field names, descriptions, values, tab order, radio-button groups, required-state semantics, or associations with instructions. Accordingly, "recovery" in this paper means geometric and type recovery, not automatic conformance with an accessibility standard.

3.2 Decision and diagnostic geometry

The operational adapter inherited from the deployment pipeline uses a symmetric containment-aware score

$$\mathrm{ov}(b, g) = \max\left(\mathrm{IoU}(b, g), \frac{|b \cap g|}{\min(|b|, |g|)}\right), \tag{2}$$

and accepts a class-consistent match when $\mathrm{ov}(b, g) \geq 0.3$. Predictions are processed in descending score order and greedily matched one-to-one within a page and class. We call the resulting precision, recall, and micro-F_1 *native* metrics. This criterion tolerates different but nested annotations of the same form cue. It can also accept an undersized box; therefore every experiment additionally reports strict IoU-0.5 operating metrics and COCO AP averaged over IoU thresholds 0.50:0.05:0.95 [8]. The strict adapter uses a stable, class-global Top-300 cap per page, whereas native evaluation may retain all 896 queries. Numbers from the two adapters are not interchangeable.

3.3 Five internal roles and an external gate

Partitioning assigns whole document groups to the *train–real*, *train–synthetic*, *development*, *calibration*, and *internal test* roles, so documents that share provenance never straddle a role boundary. Weight updates use the two training roles only. Development native containment micro-F_1 selects the exponential-moving-average checkpoint and drives early stopping. After training, calibration selects class thresholds and representative-selection parameters. The resulting candidate weights and operating point were frozen and bound by digest before internal-test inference began; that result was used for neither selection nor calibration.

A separate external corpus is quarantined behind a create-last completion record. Its assets could not be opened by the evaluation command until the candidate checkpoint, operating point, run identity, and training-completion hashes all validated. External document hashes are excluded from the training index. The decision reference is FFGBT-v8, the strongest previously accepted system on this corpus: an unpublished predecessor pipeline of the author whose sealed external report predates the present project (Section 6.3). The pre-registered decision was whether the candidate's native micro-F_1 was strictly greater than 0.82903655889853, reconstructed from that report's counts TP = 96,070, FP = 19,145, and FN = 20,478. The frozen candidate passed that gate in the single permitted external evaluation. This decision is specific to the native adapter and does not establish superiority under the separate strict adapter.

3.4 Content-addressed provenance

The run identity binds the sealed SQLite data index, model contract, pretrained checkpoint, resolved configuration, and an implementation digest covering executable Python, shell, YAML, and dependency-lock files. Every checkpoint records those values plus optimizer, scheduler, mixed-precision, distributed random-number, and early-stopping state. The candidate was copied create-once from the selected checkpoint; its digest and those of the operating point, training summary, metric history, and last checkpoint are bound into a create-only training-completion record. The external report was then written atomically with a SHA-256 sidecar and a create-only completion marker. Recomputed digests connect the final report to the same candidate and operating point that produced the post-freeze internal result. This design does not make an experiment intrinsically correct, but it prevents a reported checkpoint from silently drifting away from its registered data or implementation.

4 AcroMELD

4.1 Visual and structural evidence

4.1.1 Visual proposals

The raster branch is ECDet-L from EdgeCrafter [18], adapted from COCO to three field classes and 384 decoder queries. It produces proposal features $V \in \mathbb{R}^{384\times256}$, normalized boxes B^v, and class logits P^v. Portrait, landscape, and approximately square pages are letterboxed without cropping to 2048×1440, 1440×2048, and 1664×1664

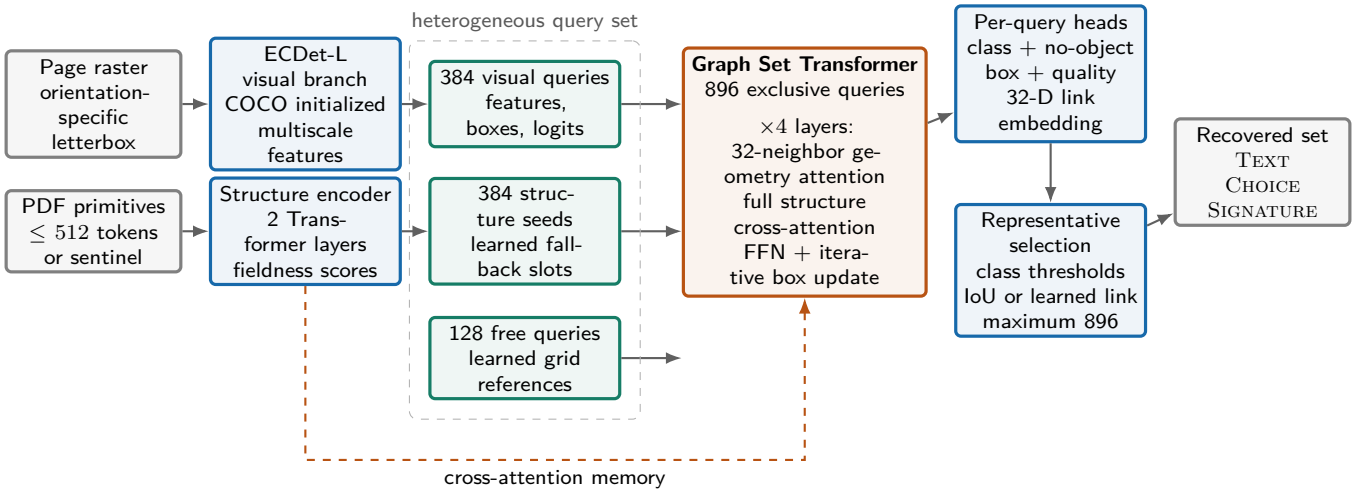

Figure 1: AcroMELD architecture. The raster and label-free PDF structure remain independent evidence channels until their heterogeneous queries enter one graph-set decoder. Dashed cross-attention makes all structure tokens available as context; solid paths produce the exclusive prediction set.

$(H \times W)$ canvases, respectively. Targets and PDF primitives use the identical transform.

4.1.2 Structure encoding

For token j, the structure encoder sums learned kind and availability embeddings, an MLP of the 32 primitive features, a box embedding, and the mean of its non-padding byte embeddings. Two pre-normalized Transformer layers contextualize the sequence. The page token supplies global context but cannot seed a field. When raw extraction yields more than 1,535 non-page primitives, a deterministic first stage preserves 12-by-12 spatial and kind coverage. A second deterministic selector retains the page token, prioritizes 16-by-16 kind coverage and form-like shapes, and caps the encoded sequence at 512 tokens.

A fieldness MLP scores each non-page token from its contextual feature, box, and log aspect ratio. The top 384 eligible tokens initialize structure queries. Missing or ineligible positions use learned fallback vectors and learned grid reference boxes; therefore the query shape is constant even when S is unavailable. Fieldness supervision marks a primitive positive when its center lies inside any target field. This signal chooses useful evidence but does not reveal a target class.

4.2 Heterogeneous query set

Let E_b be the box embedding, E_p the projected visual class logits, and e_o a source embedding. The initial visual and structural query values are

$$Q^v = V + E_b(B^v) + E_p(P^v) + e_{\text{visual}}, \tag{3}$$

$$Q^s = S_{\text{seed}} + E_b(B^s) + e_{\text{structure}}. \tag{4}$$

The 128 free values Q^f and their reference boxes are learned on a repeating grid of plausible field shapes. Concatenation yields

$$Q_0 = [Q^v; Q^s; Q^f] \in \mathbb{R}^{896\times 256}. \tag{5}$$

The three sources are not separate prediction heads: after concatenation, Hungarian assignment operates on one exclusive set. Capacity 896 follows from the data as the smallest configured source mixture that exceeds the densest page in the sealed corpus (Section 5).

4.3 Geometry-aware graph refinement

At graph layer ℓ, each query attends to the $k = 32$ query centers nearest to its current box. For ordered pair (i, j), the attention bias is learned from

$$e_{ij} = \big[\Delta x/w_i,\ \Delta y/h_i,\ \log(w_j/w_i),\ \log(h_j/h_i),\ \text{IoU}_{ij},\ e^{-|\Delta y/h_i|},\ e^{-|\Delta x/w_i|}\big]. \tag{6}$$

Eight-head sparse self-attention is followed by eight-head cross-attention from every query to all encoded structure tokens and a 1,024-dimensional feed-forward block. Residual connections, pre-normalization, GELU activations, and dropout 0.1 are used throughout. The sparse attention aggregation stores $O(Qk)$ edges; the current exact nearest-neighbor search computes an $O(Q^2)$ center-distance matrix. This distinction matters when considering larger future query sets.

Each of four layers adds a box delta in inverse-sigmoid coordinates, clamps the result to valid normalized boxes, and emits auxiliary class, box, and quality predictions. Iterative geometry therefore changes the graph neighborhood seen by the next layer.

4.4 Set, quality, and relation objectives

Hungarian assignment uses class, L1-box, and generalized-IoU costs with weights $(2, 5, 2)$ [7, 10]. For matched final queries, the corresponding loss weights are also $(2, 5, 2)$, with class weights $(1, 1.5, 4)$ for TEXT, CHOICE, and SIGNATURE, and no-object weight 0.08. Earlier graph layers receive the same set loss with geometric decay 0.65. The native ECDet criterion is retained at weight 0.5 so the visual proposal interface remains directly supervised.

The quality target for a matched prediction is the detached ov value in Equation (2). Binary cross entropy trains one quality logit r_i; background queries are down-weighted as confidence becomes small. Inference ranks query i by

$$s_i = \sqrt{\max_c p_{ic}\, \sigma(r_i)}, \tag{7}$$

aligning score order with both classification and the declared localization decision. L1 and generalized-IoU losses continue to penalize imprecise containment.

The link head maps final queries to unit-normalized 32-dimensional vectors z_i. It predicts

$$p_{ij}^{\text{link}} = \sigma(z_i^\top z_j / 0.1). \tag{8}$$

Supervision covers unordered pairs that could interact during decoding: those with IoU ≥ 0.05 or ov ≥ 0.3. A pair is positive exactly when both boxes overlap the same ground-truth field by at least 0.3; class is not part of this label. Weighted binary cross entropy handles the positive/negative imbalance. Relation and fieldness losses each carry weight 0.2.

4.5 Containment-aware representative selection

Candidates below a raw score floor of 0.01 are discarded. At a calibrated operating point, a remaining candidate is eligible only if its score meets the threshold for its predicted class. Eligible candidates then enter a stable descending-score greedy selection. A selected representative suppresses candidate j if either their IoU meets or exceeds τ_{nms}, or they satisfy the same spatial gate used for relation supervision and $p_{ij}^{\text{link}} \geq \tau_{\text{link}}$. Suppression is deliberately class-agnostic: two sources may disagree on type while still referring to one field. The selected set is capped at 896 fields per page.

5 Data and Training

5.1 Sealed corpus

The internal corpus contains 35,388 PDFs, 119,418 pages, and 2,550,287 spatially valid widgets. Existing native widgets provide supervision, while the model input is rendered without exposing their metadata through the structure channel. The index rejects degenerate or off-page boxes outright, without inventing replacement geometry: 2,295 text, 77 choice, and 798 signature widgets from source manifests were excluded by this rule. Splits are made over indivisible provenance groups and have no content-hash crossing. The exact post-validation counts are shown in Table 1.

The maximum is 849 fields on one real training page; every split remains below the 896-query capacity. Empty pages are retained, including 23,607 real training pages, because false positive behavior is part of deployment. Structure is available for 91,637 pages. The remainder, including every synthetic page, tests the same visual-only path used for scans.

The 15,785 synthetic pages come from 5,000 generated PDFs. They are rendered with widgets disabled, preventing the appearance of a native widget from leaking into its own input image. Synthetic pages contribute no PDF primitive tokens. Real signature-bearing pages are sampled with weight three, while synthetic pages remain at unit weight; this improves rare-class exposure without allowing the generator distribution to dominate. The corpus cannot be redistributed with the code because source-document rights vary; hashes, contracts, and aggregate statistics are retained for audit instead.

5.2 Augmentation and missing structure

Page geometry is preserved. Images may be scaled by 0.92–1.00 and translated within the letterbox, followed by brightness/contrast perturbation, blur, JPEG degradation, and sensor noise. Flips, mosaics, mixup, arbitrary crops, and rotations are disabled because they can change form semantics or remove fields. Raster, boxes, and structure receive one shared geometric transform. During training, all structure is dropped on 12% of pages and 5% of non-page tokens are independently dropped; the page sentinel remains. This creates a declared visual fallback instead of a hidden zero-filled special case.

5.3 Optimization

The registered run uses AdamW with $(\beta_1, \beta_2) = (0.9, 0.999)$, weight decay 10^{-4}, BF16 autocasting, gradient-norm clipping at 0.1, and exponential-moving-average decay 0.9998. Learning rates are 2×10^{-4} for the graph/structure modules, 10^{-4} for the remaining visual branch, and 4×10^{-6} for the backbone. The backbone is frozen for the first two epochs. After 1,500 warm-up steps, cosine decay reaches 5% of each base rate by epoch 30.

Training uses two NVIDIA RTX A6000 GPUs. An empirical worst-case forward/backward trial on a 2048×1440 page with 849 targets and 512 structure tokens selected four pages per device; gradient accumulation of four and two distributed ranks produce an effective batch of 32. The selected trial allocated 22.10 GiB per GPU; batch eight allocated 44.57 GiB and was rejected by the reserve policy. Each completed epoch contains 3,087 optimizer steps.

Table 1: Sealed internal data roles. "Structure" counts pages with extracted PDF primitives; pages without structure use the same unavailable sentinel. Training rows are the only rows used for gradient updates.

Role	PDFs	Pages	Structure	TEXT	CHOICE	SIGNATURE	All fields
Train–real	21,272	72,548	61,332	1,356,974	319,535	6,117	1,682,626
Train–synthetic	5,000	15,785	0	120,456	17,550	7,842	145,848
Development	2,281	7,748	7,726	145,174	34,165	638	179,977
Calibration	758	2,612	2,612	48,916	11,497	233	60,646
Internal test	6,077	20,725	19,967	388,184	91,318	1,688	481,190
Total	35,388	119,418	91,637	2,059,704	474,065	16,518	2,550,287

Main training was registered for at least seven and at most 30 epochs. Every strict improvement in development native-containment micro-F_1 saved the best EMA checkpoint; patience of five used a separate minimum increment of 0.0005. The run reached the 30-epoch main-phase cap without triggering patience. The terminal phase then reloaded the best EMA checkpoint, cleared optimizer state, disabled augmentation, reduced every learning rate by a factor of ten, and completed its three registered epochs. Training ended at that terminal cap after 33 epochs; the final record, after completed epoch 33, was also the best EMA checkpoint and became the frozen candidate. The registered selection metric was still improving, leaving convergence unresolved. All reported results come from this single run, so run-to-run stability remains unmeasured.

The full model has 39,375,424 trainable parameters. The visual branch contributes 32,846,939 (83.4%); the structure encoder and graph-set decoder contribute 6,528,485 (16.6%). Parameter transfer from the published ECDet-L checkpoint covers 99.9969% of compatible visual parameters; the three-class score heads are initialized from the mean COCO class weights, while the visual denoising class embedding is the only compatible visual tensor left random.

6 Evaluation Design

6.1 Operating-point calibration

Calibration was a discrete, deterministic search performed only after the best EMA checkpoint and terminal phase were fixed. The representative-selection grid was the Cartesian product of

$$\tau_{\text{nms}} \in \{0.30, 0.50, 0.70, 0.80, 0.85, 0.90, 0.95, 1.00\},$$
$$\tau_{\text{link}} \in \{0.50, 0.65, 0.80, 0.90, 0.95, 1.00\}.$$

The $(1, 1)$ point is near-unsuppressed rather than suppression-free: the decoder uses inclusive comparisons, so exact-one IoU or link probabilities may still suppress a candidate. For each of the 48 decoder points, class thresholds were selected jointly from 981 descending values between 0.99 and 0.01 at resolution 0.001. An exact finite fractional optimizer maximized native containment micro-F_1 without materializing the cubic threshold grid. Integer cross-products avoided floating-point disagreement; ties preferred higher class thresholds and then the least-aggressive representative settings.

The selected thresholds were $(0.769, 0.812, 0.990)$ for TEXT, CHOICE, and SIGNATURE, with $(\tau_{\text{nms}}, \tau_{\text{link}}) = (1.000, 0.950)$. Forty of the 48 grid cells (all eight NMS values paired with any of the five registered link thresholds below 1.00) shared the same aggregate native calibration F_1 and optimized class thresholds, even though their retained prediction sets may differ. The registered tie-break selected the least-aggressive member of that set. The eight cells with link threshold 1.00 scored lower. Because the model weights remained fixed, this grid measures operating-point sensitivity; it cannot speak to the contribution of relation learning. The resulting JSON operating point was hash-bound to the candidate checkpoint before internal-test inference.

6.2 Internal and external reports

Internal-test inference began only after the candidate and operating point were sealed, and the internal test was used for neither checkpoint selection nor calibration. Its report contains native micro and per-class counts, precision, recall, and F_1, together with strict IoU-0.5 counts, COCO mAP, AP_{50}, AP_{75}, and classwise AP. Native containment AP was not emitted for the internal split and is therefore not claimed. The identical frozen candidate and operating point were subsequently evaluated once on the external holdout of 1,996 PDFs and 6,843 pages.

After the sealed point result, 10,000 percentile-bootstrap resamples clustered by PDF and using seed 12345 quantified descriptive uncertainty. The same frozen external predictions also supported descriptive strata by field-count density, vector-primitive availability, page orientation, class, and target-empty pages. Neither the intervals nor the strata affected selection, calibration, or the registered pass/fail decision. The sealed detection shards do not retain query-origin or individual suppression-decision provenance, so those two diagnostics cannot be reconstructed and are not reported.

6.3 External corpus, references, and comparability

6.3.1 Corpus provenance and composition

The external holdout is the frozen validation benchmark of an unpublished predecessor form-recovery project by the author. It predates the present project, was inherited read-only as a hash-bound snapshot, and is the cleaned revision, at 1,996 documents, of an earlier 2,290-document collection; every document hash is excluded from the training index (Section 3.3). Ground truth is derived exactly as for the internal corpus: the documents already carry native AcroForm widgets, whose extracted geometry and coarse type form the native-adapter targets, while a separately maintained COCO file provides the strict annotations. The corpus spans 6,843 pages with 116,548 native widgets (77,858 Text, 37,221 Choice, and 1,469 Signature) and 116,542 strict annotations. 1,439 pages contain no target field, 388 pages expose no vector primitives, and no page exceeds 300 fields. Page rasters are pre-rendered with interactive widget appearance disabled under the same rendering contract as training, and structure tokens come from the same label-free extraction. The documents are third-party material under mixed licenses, so the corpus itself cannot be released. Language, jurisdiction, and document-domain composition were inherited without further annotation and are characterized only through the descriptive strata in Section 7, a limitation Section 8 records.

6.3.2 Native decision reference

FFGBT-v8 (FFGBT/LightGBM version 8 with SnapNet-E3 refinement) is the strongest previously accepted system on this benchmark, which is why it was registered as the pass/fail reference before training began. Architecturally it is unrelated to AcroMELD: deterministic candidate boxes derived from PDF-structure primitives and whitespace analysis are scored by gradient-boosted trees, accepted boxes pass a refinement network, and output is truncated to 300 detections per page. Its sealed report on the identical corpus and native adapter records TP = 96,070, FP = 19,145, and FN = 20,478 (micro-F_1 0.8290), with classwise F_1 of 0.810 for Text, 0.891 for Choice, and 0.121 for Signature. The pipeline is unpublished, and its per-document predictions were not retained; only these aggregate and classwise counts document it, which precludes any paired candidate–baseline uncertainty estimate (Section 7).

6.3.3 Strict reference

The strict adapter's CommonForms-L/FFDNet-L reference is a local evaluation of the released detector, not the result reported by CommonForms on its own test corpus [6]. That local run reached micro-F_1 0.8014 at IoU 0.5 and three-class COCO mAP 0.3410. These references provide adapter-specific context rather than a joint ranking: native containment and strict IoU use different annotations, matching rules, and caps. We therefore compare AcroMELD with each reference only under the corresponding adapter and do not compare the two reference values with one another.

Table 2: Evaluation adapters. Only the native external row bears the registered decision.

Adapter	Match	Per-page cap	Purpose
Native	ov ≥ 0.3	896	selection/gate
Strict operating	IoU≥ 0.5	300	localization
Strict COCO	IoU sweep	300	diagnostic AP

6.4 Evidence boundary

The study evaluates one registered training trajectory and its frozen system. It includes neither retrained component ablations nor post-freeze interventions that remove structure or link-based selection. The calibration grid measures decoder sensitivity for fixed weights; naturally occurring vector-availability and density strata are confounded by document source and visual characteristics. Isolating the effects of structure seeds, free queries, relation supervision, or containment-quality supervision requires a controlled intervention. The reported evidence is therefore system-level.

7 Results

7.1 Training trajectory and candidate selection

The registered run completed 33 epochs: 30 main-training epochs followed by three augmentation-free finale epochs. Figure 2 shows the development measurements used for checkpoint selection. These measurements retain the training-time decoder point $(\tau_{\text{nms}}, \tau_{\text{link}}) = (0.90, 0.80)$ and class thresholds $(0.3, 0.3, 0.3)$; they are neither calibrated results nor estimates of held-out performance. Native micro-F_1 rose from 0.760 after the first completed epoch to 0.8956 after epoch 33, while strict IoU-0.5 micro-F_1 reached 0.8564 and strict COCO mAP reached 0.7243.

The final record, with zero-based index 32, was also the selected EMA checkpoint. The run reached the pre-registered finale epoch cap while native development F_1 had increased for five consecutive epochs. The development trajectory was therefore still improving at termination.

7.2 Calibration and post-freeze evaluation

Calibration selected class thresholds $(0.769, 0.812, 0.990)$ for Text, Choice, and Signature, respectively, with

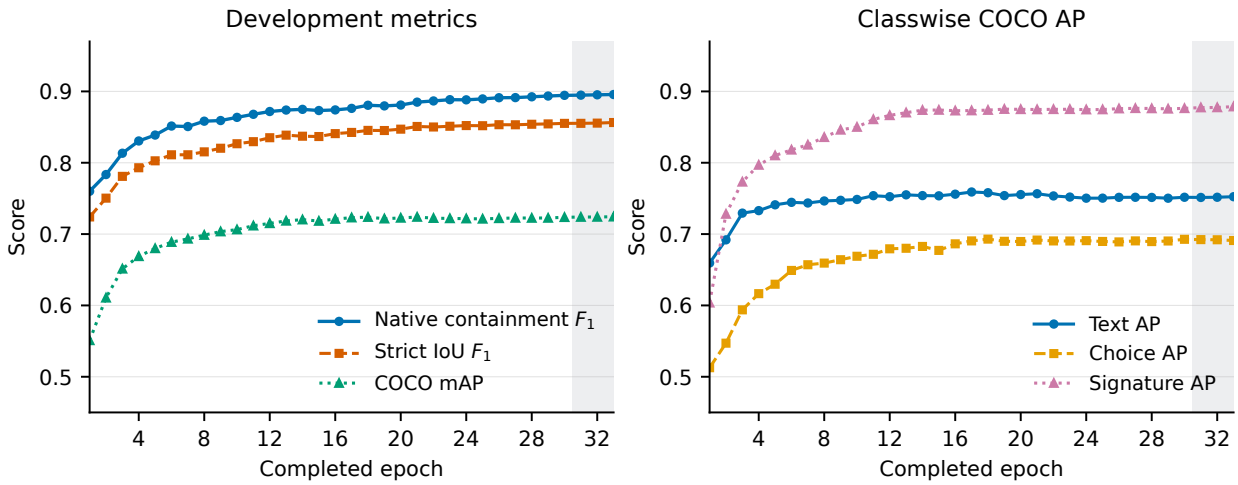

Figure 2: Development trajectory across 33 completed epochs at the fixed training-time decoder point. Left: native containment F_1, strict IoU-0.5 F_1, and strict COCO mAP. Right: classwise strict COCO AP. Shading marks the three augmentation-free finale epochs. These repeatedly observed development measurements drove checkpoint selection and are not held-out learning curves.

$(\tau_{\text{nms}}, \tau_{\text{link}}) = (1.000, 0.950)$. The selected native calibration micro-F_1 was 0.9269. The decoder grid was highly degenerate: all 40 cells with $\tau_{\text{link}} < 1$ produced the same aggregate calibration micro-F_1 and selected class thresholds across the complete NMS grid. The registered tie-break chose the least-aggressive tied point. As Section 6 specifies, this fixed-weight search selects an operating point but cannot measure the benefit of learned linking.

Table 3 reports the decision-bearing native adapter. Here and below, *fixed 0.3* changes only the three class thresholds to $(0.3, 0.3, 0.3)$; it retains the same sealed candidate and calibrated NMS/link settings. Development and calibration rows are included to disclose their roles; only the internal and external rows are post-freeze estimates.

At the selected point, the external native micro-F_1 of 0.8477 exceeded the registered historical FFGBT-v8 value 0.8290 by 0.0186, and therefore passed the registered one-shot gate. A 10,000-resample PDF-cluster bootstrap, computed only after the sealed point result, gives the descriptive interval $[0.8339, 0.8605]$ for the candidate's external F_1. This interval describes variation across the evaluated candidate documents; it is not a confidence interval for the candidate–baseline margin because no corresponding clustered baseline predictions are available.

The fixed-0.3 control reached only 0.7770, with descriptive interval $[0.7608, 0.7918]$. Thus class-threshold calibration changed external F_1 by 0.0707 for the same candidate and representative settings. Only aggregate results survive for FFGBT-v8, so the equivalence of its threshold-tuning procedure cannot be assessed.

Strict results tell a less favorable but complementary story (Table 4). On the external strict adapter, AcroMELD reached micro-F_1 0.7786 at the selected class thresholds and strict COCO mAP 0.2900. Both its strict operating-point F_1 and three-class mAP are below the local CommonForms-L references of 0.8014 and 0.3410, respectively. These strict values use 116,542 annotations and a Top-300 cap, placing them outside the native gate comparison.

7.3 Class behavior and descriptive strata

The aggregate external result conceals a zero-recall outcome on Signature (Table 5). The selected threshold produced no external signature predictions, so signature precision is undefined rather than zero; recall and F_1 are zero. Lowering only the class thresholds to 0.3 raised signature F_1 to merely 0.0677. The class-threshold-free strict signature AP also fell from 0.8787 on development to 0.5798 on internal test and 0.0023 externally. The high calibrated threshold directly caused zero selected predictions. The weak fixed-threshold F_1 and strict AP show that thresholding alone cannot account for the transfer failure.

The selected native result drops by 0.0867 from internal test to external holdout at the same operating point. Post-freeze descriptive strata contextualize this gap without assigning a cause. External F_1 was 0.7505 on pages with 1–10 fields, 0.8688 with 11–100, and 0.9044 with 101–300; no page in the external corpus holds more than 300 fields, so a potential dense-page advantage of the 896-query capacity remains untested. Pages with vector primitives reached 0.8505, compared with 0.7094 on the 388 pages without them. Because vector availability tracks scan status, document source, and visual style (Section 6.4), the contrast is not a causal estimate of the structure contribution.

Orientation results were 0.8528 for portrait and 0.8225 for landscape pages. The square-page value 0.9512 is

Table 3: Native containment results (ov ≥ 0.3, maximum 896 detections per page). "Selected" denotes the calibration-only class thresholds; the fixed-0.3 external control changes only those class thresholds. The FFGBT-v8 row is the registered historical external reference used by the pre-registered gate.

Corpus	Point	Precision	Recall	Micro-F_1	TP	FP	FN
Development	selected	0.9485	0.9229	0.9355	166,107	9,023	13,870
Calibration	selected	0.9516	0.9035	0.9269	54,792	2,784	5,854
Internal test	selected	0.9478	0.9214	**0.9344**	443,366	24,437	37,824
External	selected	0.8592	0.8364	**0.8477**	97,486	15,974	19,062
External	fixed 0.3	0.6900	0.8890	0.7770	103,616	46,550	12,932
External	FFGBT-v8	0.8338	0.8243	0.8290	96,070	19,145	20,478

Table 4: Strict localization diagnostics. Operating F_1 uses IoU$\geq$ 0.5; mAP uses the COCO IoU sweep. CommonForms-L mAP is the recorded three-class aggregate; comparable three-class AP_{50} and AP_{75} aggregates were not recorded.

Corpus / point	F_1	mAP	AP_{50}	AP_{75}
Internal / selected	0.9042	0.6467	0.7792	0.7062
External / selected	0.7786	0.2900	0.4903	0.2772
External / fixed 0.3	0.7017	—	—	—
External / CommonForms-L	0.8014	0.3410	—	—

based on only 33 pages. Of 1,439 target-empty pages, 242 contained at least one false positive (16.82%); averaged over all empty pages, the model emitted 2.6192 false positives per page. All intervals and strata were computed after candidate freezing and did not feed back into model, threshold, or gate selection.

8 Discussion and Limitations

8.1 Interpreting the registered result

The sealed candidate passed the pre-registered native gate at its calibration-only operating point. That result is specific to the declared adapter and calibration procedure. With fixed 0.3 class thresholds, the same candidate scored 0.7770, below FFGBT-v8; only aggregate baseline results survive, so equivalent threshold tuning cannot be verified. Under strict IoU-0.5 evaluation, AcroMELD also remained below the local CommonForms-L reference. The experiment thus supports the registered operational decision without establishing a general detector ranking.

Calibration increased external native F_1 by 0.0707 through a precision–recall trade, including a conservative 0.990 signature threshold. The 40 tied NMS/link grid cells identify no preferred suppression setting, and their fixed weights preclude component attribution. An explicit no-link intervention or retrained relation ablation is still needed to test the same-field mechanism.

8.2 Generalization and signature failure

The 0.0867 internal-to-external F_1 gap at one frozen operating point shows that the internal test is not a reliable proxy for this external domain. The strongest failure is Signature: selected external recall and F_1 are zero, and both the fixed-threshold result and class-threshold-free strict AP remain very low. Signature-bearing development documents are highly concentrated in one indivisible provenance group, while synthetic signatures introduce a separate rendering distribution. Either could contribute to the gap, but this experiment cannot distinguish them. Future work requires provenance-diverse real signatures and group-aware evaluation rather than further tuning on this holdout.

8.3 Component and capacity evidence

Born-digital primitives offer precise geometry without guaranteed semantic relevance. Dropout and fallback queries preserve a visual-only path, but the vector-present stratum compares different document populations; the same pages were never evaluated with and without structure. The experiment contains no controlled structure-removal or capacity-matched retraining, so the system-level result cannot isolate the contributions of structure seeds, free queries, relation supervision, or containment-quality supervision.

Performance increased across the observed positive-page density strata, but the external holdout never exceeds 300 fields per page. The 896-query capacity therefore guards against the truncation measured internally; whether it helps externally over a Top-300 cap cannot be observed here.

8.4 Data and metric limitations

Supervision is derived from existing native widgets. Such widgets can be inaccurate, duplicated, or inconsistent with visible cues, and they overrepresent documents that were already interactive. The corpus itself cannot be shared (Section 5), which limits independent replication of exact training. Language, jurisdiction, document-domain, and collection-time distributions have not been comprehensively quantified. One registered seed provides no estimate of optimization variance.

Containment overlap is useful when two annotations cover the same cue at different extents, yet its second term can assign a perfect score to a very small box entirely

Table 5: Classwise results. Internal F_1 and all external P/R/F_1 values use the selected native operating point. External overlap AP and strict COCO AP are class-threshold-free ranking diagnostics under their respective adapters. Signature precision is undefined because no signature prediction survived the selected class threshold.

Class	Internal F_1	External P	External R	External F_1	Overlap AP	Strict AP
Text	0.9405	0.8455	0.8247	0.8350	0.8234	0.5005
Choice	0.9126	0.8870	0.8939	0.8904	0.9133	0.3782
Signature	0.5498	—	0.0000	0.0000	0.0071	0.0023

inside a target. Strict IoU losses and metrics guard against favorable but imprecise native scores. Because the two adapters use different ground truth and caps, the native bootstrap intervals describe only the candidate under native matching; they do not quantify strict performance or the candidate–baseline margin.

8.5 Scope, efficiency, and data responsibility

Detected boxes and coarse classes do not make a form accessible or semantically correct. False positive widgets can obscure content, false negatives preserve an access barrier, and an incorrect choice/text type changes interaction behavior. A production system should expose confidence, preserve the original PDF, and require human review before publication. Field labels, descriptions, group semantics, keyboard order, language, error instructions, and assistive-technology testing remain separate remediation tasks [4]. AcroMELD does not generate JavaScript or infer document values.

The false positives on target-empty pages illustrate this operational boundary: 16.82% of such pages received at least one prediction. A remediation workflow therefore needs both abstention and human review.

The two-rank external inference pass processed 6,843 pages at an aggregate 24.39 pages/s and recorded 3.03 GiB peak allocated GPU memory per rank on two RTX A6000 GPUs. This whole-corpus throughput is not batch-one latency. The model uses high-resolution canvases, 39.4M parameters, and 896 queries; energy and single-page latency remain unmeasured. Pages above 896 fields exceed the training contract and are truncated during decoding.

PDFs may contain names or other personal information even when publicly obtainable. The model does not require target values: structure text is truncated to 48 bytes and used only as an input feature, while source documents are not distributed with the repository. This containment does not replace a full data-protection and licensing review before releasing weights or a service.

9 Conclusion

We presented AcroMELD, a structure-aware graph set transformer for recovering the geometry and coarse type of missing PDF form widgets. The method keeps three complementary proposal sources in one 896-query exclusive set, refines them through sparse geometry-aware interactions and PDF cross-attention, and learns both containment-aligned localization quality and same-field links. The experimental protocol binds capacity, adapter semantics, calibration, and artifact lineage to the reported result.

After 33 epochs, calibration fixed one operating point before either test role was opened. Native micro-F_1 reached 0.9344 internally and 0.8477 externally, passing the historical FFGBT-v8 gate by 0.0186. However, strict external performance (0.7786 IoU-0.5 F_1 and 0.2900 COCO mAP) trailed the local CommonForms-L reference, and no signature prediction survived the selected threshold. The operational gain therefore coexists with a clear domain-transfer and rare-class failure. Further runs and controlled ablations are needed to determine which architectural components account for the system-level result.

Table 6: Trainable parameter allocation.

Component	Parameters	Share
Visual backbone	22,463,664	57.1%
Other visual modules	10,383,275	26.4%
Structure encoder	1,789,184	4.5%
Four graph layers	4,221,984	10.7%
Query/seed embeddings	235,649	0.6%
Graph output heads	281,668	0.7%
Total	39,375,424	100.0%

A Implementation and Run Contract

A.1 Parameter accounting

The registered model contract is hidden width 256, eight heads, structure depth two, graph depth four, feed-forward width 1,024, 384 visual queries, 384 structure queries, 128 free queries, 32 graph neighbors, and link width 32. There are 23,852 non-trainable buffers. The query contract fails closed during training if a page contains more targets than queries.

A.2 Completed run identity

The registered run completed 30 main-phase and three augmentation-free finale epochs. The last record, zero-

indexed epoch 32, was also the selected checkpoint; termination was the registered `finale_epoch_cap`, not a test-dependent stopping decision. Training used seed 3407, two RTX A6000 devices, distributed BF16, per-device batch four, gradient accumulation four, and effective global batch 32. No AMP overflow was recorded in any of the 33 complete metric rows. The principal identities are:

- sealed index: `8d978c02830b...89c20ede`;
- implementation: `38b86053e40b...46e6d10`;
- resolved run configuration: `fd1519e7a787...9c29a2`;
- model contract: `8b78a265efd7...56bf20`;
- pretrained ECDet-L: `60e48c51b33d...1e85a1`; and
- frozen candidate: `878f94ee9316...a8e4dd87`.

The implementation digest is reproduced by repository commit `227b9a6d651aa882a4776579eb56d15104b8c269`. The current manuscript checkout contains later dependency changes and consequently has a different implementation digest. Appendix B records the complete artifact digests and their binding chain.

A.3 Complete development trajectory

The trajectory uses the registered diagnostic decoder: class thresholds $(0.3, 0.3, 0.3)$ and $(\tau_{\text{nms}}, \tau_{\text{link}}) = (0.90, 0.80)$. The development row in Table 3 is a separate re-evaluation of the same frozen candidate with the calibration-selected class thresholds and representative parameters. Its native F_1 is therefore not directly comparable with the trajectory's final value 0.8956.

A.4 Decoder controls

Calibration selected class thresholds $(0.769, 0.812, 0.990)$ and $(\tau_{\text{nms}}, \tau_{\text{link}}) = (1.000, 0.950)$. The search covered 48 NMS/link cells and 981 class-threshold values per cell. Forty cells attained the same aggregate calibration F_1 and class thresholds; the registered tie break selected the least-aggressive corner among those tied cells. This point is *near-unsuppressed*: inclusive comparisons still remove identical boxes at IoU 1 or candidates with sufficiently confident links. Aggregate ties may also retain different prediction sets. The search specifies a decoder operating point; attributing an effect to NMS or link suppression requires an intervention.

Table 7: All 33 development evaluations. Rows 1–30 are the main phase and rows 31–33 the augmentation-free finale. The accompanying CSV retains precision, recall, class AP, loss, phase, and evaluation time.

Epoch	Native F_1	Strict F_1	mAP	AP_{50}
1	0.760	0.724	0.551	0.785
2	0.783	0.750	0.611	0.829
3	0.813	0.781	0.651	0.853
4	0.831	0.793	0.669	0.855
5	0.839	0.803	0.680	0.861
6	0.851	0.811	0.689	0.865
7	0.851	0.811	0.693	0.865
8	0.858	0.815	0.699	0.862
9	0.859	0.820	0.703	0.864
10	0.864	0.827	0.706	0.867
11	0.868	0.830	0.712	0.869
12	0.872	0.835	0.715	0.869
13	0.874	0.839	0.718	0.870
14	0.875	0.837	0.720	0.871
15	0.873	0.837	0.718	0.869
16	0.874	0.841	0.721	0.870
17	0.876	0.843	0.723	0.871
18	0.881	0.845	0.724	0.870
19	0.880	0.845	0.722	0.870
20	0.881	0.847	0.723	0.869
21	0.885	0.851	0.724	0.869
22	0.887	0.850	0.722	0.869
23	0.888	0.851	0.722	0.869
24	0.888	0.852	0.722	0.869
25	0.889	0.852	0.721	0.869
26	0.891	0.853	0.722	0.869
27	0.891	0.853	0.723	0.869
28	0.892	0.854	0.723	0.869
29	0.894	0.854	0.723	0.869
30	0.894	0.855	0.724	0.869
31	0.895	0.855	0.724	0.869
32	0.895	0.856	0.724	0.869
33	0.896	0.856	0.724	0.870

B Artifact Record, Availability, and Declarations

B.1 Hash-bound final record

The create-last completion record binds the frozen candidate to the full metric history, selected operating point, training summary, resolved configuration, implementation, sealed index, model contract, and pretrained checkpoint. The external identity then binds that completed run to the quarantined corpus and adapter contract; the external report binds itself to that identity, and a separate completion marker binds the report digest. The following complete SHA-256 identities distinguish this result from any later rerun or manuscript revision:

- `candidate.pt`: `878f94ee93162807109c38f3b06bc7398b03ba315452ea3c7a3b384ca8e4dd87`
- `metrics.jsonl`: `e5b3359d444f81e173a8196ba14746171dca85bacba7ba71728d6cf2689627d8`
- `operating-point.json`: `59961703552d3b6f5c505008981f356b3b65f69b912ccebf0fa49b7d6891ee14`
- `training-summary.json`: `9aa588369c1cb880c63f01d16e82f7f69d6d8a500370e54317df2bf75c159eab`
- `training-complete.json`: `df915c6a9d85642dd207d4200f65701170fe30b0ff908a12f192432cf4352495`

- run-identity.json: 1bd33553ca2fa3604f4b323e93d4c0db3a61a1262ade70495602208c9da2ca21
- external run identity: 6f896463d5626979452e32a3bcabcbbb32dae6575d112626dd08caf1ddb6994b
- external report: 903a20a71a7631aeb6f2e7e0b27ee966510b2a7e88ee7fdca571040a4bde7b84
- external completion marker: 613335b79d1027459603a7da82d461b43110320e987c9beb12643012181a3164
- post-freeze analysis: 4eb25ebb9e6d7c008b08de8bafbb1096971e6213404fd105198595e3b60bfed1
- prediction shard, rank 0: 1c490926971ffe71969ba0121f3083a7defdd23d7380416c8a7f66c4026b16b6
- prediction shard, rank 1: fcc9196b060867a81fbf3cba6923eedc259844eba6116082d9f7c933ab0a6a76

The repository manifest covers every compact artifact copied into the paper evidence snapshot. The paper generator pins the manifest contents, recomputes each digest, checks the cross-artifact bindings above, and fails closed before producing tables or figures. The report's `.sha256` sidecar stores the bare 64-character digest; the two-column `SHA256SUMS` file is the canonical input for `sha256sum -c`. The post-freeze analysis is descriptive only: it validates the source PDFs and both prediction shards, then reconstructs the sealed point counts before calculating PDF-cluster intervals and strata. It was not used for selection or calibration.

B.2 Availability

The source repository is private at the time of writing and no public archival release or DOI is claimed. The trained weights and source PDF corpus are also not publicly distributed. The sealed candidate and its verification artifacts (operating point, per-epoch history, external report, and every seal digest) are held in a private archive and can be made available for hash audit on request. The corpus contains third-party documents with heterogeneous redistribution rights and potentially sensitive content; releasing either corpus-derived model artifacts or predictions requires a rights and data-protection assessment. Thus the hashes, aggregate results, contracts, and deterministic derivation procedure support audit of the reported record, but an independent exact rerun is not currently possible from public materials alone.

B.3 Author contribution and competing interest

Samuel Abramov designed and implemented the system, curated the experimental protocol, conducted the experiments, analyzed the results, and wrote the manuscript. Abramov is affiliated with Accessful GmbH; because the work concerns document-accessibility technology, this affiliation is disclosed as a potential competing interest.

References

[1] World Wide Web Consortium. PDF3: Ensuring correct tab and reading order in PDF (Portable Document Format) documents. Web Content Accessibility Guidelines 2.2 Technique, 2025. URL https://www.w3.org/WAI/WCAG22/Techniques/pdf/PDF3.html. Accessed 3 August 2026.

[2] World Wide Web Consortium. PDF12: Providing name, role, value information for form fields in PDF documents. Web Content Accessibility Guidelines 2.2 Technique, 2025. URL https://www.w3.org/WAI/WCAG22/Techniques/pdf/PDF12.html. Accessed 3 August 2026.

[3] World Wide Web Consortium. PDF22: Indicating when user input falls outside the required format or values in PDF forms. Web Content Accessibility Guidelines 2.2 Technique, 2026. URL https://www.w3.org/WAI/WCAG22/Techniques/pdf/PDF22.html. Accessed 3 August 2026.

[4] World Wide Web Consortium. PDF23: Providing interactive form controls in PDF (Portable Document Format) documents. Web Content Accessibility Guidelines 2.2 Technique, 2025. URL https://www.w3.org/WAI/WCAG22/Techniques/pdf/PDF23.html. Accessed 3 August 2026.

[5] International Organization for Standardization. ISO 32000-2:2020: Document management—Portable document format—Part 2: PDF 2.0. International Standard, 2020. URL https://www.iso.org/standard/75839.html.

[6] Joe Barrow. CommonForms: A large, diverse dataset for form field detection. *arXiv preprint arXiv:2509.16506*, 2025. URL https://arxiv.org/abs/2509.16506.

[7] Nicolas Carion, Francisco Massa, Gabriel Synnaeve, Nicolas Usunier, Alexander Kirillov, and Sergey Zagoruyko. End-to-end object detection with transformers. In *European Conference on Computer Vision (ECCV)*, pages 213–229, 2020. URL https://arxiv.org/abs/2005.12872.

[8] Tsung-Yi Lin, Michael Maire, Serge Belongie, Lubomir Bourdev, Ross Girshick, James Hays, Pietro Perona, Deva Ramanan, C. Lawrence Zitnick, and Piotr Dollár. Microsoft COCO: Common objects in context. In *European Conference on Computer Vision (ECCV)*, pages 740–755, 2014. URL https://arxiv.org/abs/1405.0312.

[9] Borui Jiang, Ruixuan Luo, Jiayuan Mao, Tete Xiao, and Yuning Jiang. Acquisition of localization confidence for accurate object detection. In *European Conference on Computer Vision (ECCV)*, pages 816–832, 2018. URL https://arxiv.org/abs/1807.11590.

[10] Hamid Rezatofighi, Nathan Tsoi, JunYoung Gwak, Amir Sadeghian, Ian Reid, and Silvio Savarese. Generalized intersection over union: A metric and a loss for bounding box regression. In *IEEE/CVF Conference on Computer Vision and Pattern Recognition (CVPR)*, pages 658–666, 2019. URL https://arxiv.org/abs/1902.09630.

[11] Guillaume Jaume, Hazim Kemal Ekenel, and Jean-Philippe Thiran. FUNSD: A dataset for form understanding in noisy scanned documents. In *International Conference on Document Analysis and Recognition Workshops (ICDARW)*, volume 2, pages 1–6, 2019. URL https://arxiv.org/abs/1905.13538.

[12] Xu Zhong, Jianbin Tang, and Antonio Jimeno Yepes. PubLayNet: Largest dataset ever for document layout analysis. In *International Conference on Document Analysis and Recognition (ICDAR)*, pages 1015–1022, 2019. URL https://arxiv.org/abs/1908.07836.

[13] Birgit Pfitzmann, Christoph Auer, Michele Dolfi, Ahmed S. Nassar, and Peter W. J. Staar. DocLayNet: A large human-annotated dataset for document-layout segmentation. In *ACM SIGKDD Conference on Knowledge Discovery and Data Mining (KDD)*, pages 3743–3751, 2022. URL https://arxiv.org/abs/2206.01062.

[14] Yiheng Xu, Minghao Li, Lei Cui, Shaohan Huang, Furu Wei, and Ming Zhou. LayoutLM: Pre-training of text and layout for document image understanding. In *ACM SIGKDD International Conference on Knowledge Discovery and Data Mining (KDD)*, pages 1192–1200, 2020. URL https://arxiv.org/abs/1912.13318.

[15] Yupan Huang, Tengchao Lv, Lei Cui, Yutong Lu, and Furu Wei. LayoutLMv3: Pre-training for document AI with unified text and image masking. In *ACM International Conference on Multimedia (ACM MM)*, pages 4083–4091, 2022. URL https://arxiv.org/abs/2204.08387.

[16] Srikar Appalaraju, Bhavan Jasani, Bhargava Urala Kota, Yusheng Xie, and R. Manmatha. DocFormer: End-to-end transformer for document understanding. In *IEEE/CVF International Conference on Computer Vision (ICCV)*, pages 973–983, 2021. URL https://arxiv.org/abs/2106.11539.

[17] Xizhou Zhu, Weijie Su, Lewei Lu, Bin Li, Xiaogang Wang, and Jifeng Dai. Deformable DETR: Deformable transformers for end-to-end object detection. In *International Conference on Learning Representations (ICLR)*, 2021. URL https://arxiv.org/abs/2010.04159.

[18] Longfei Liu, Yongjie Hou, Yang Li, Qirui Wang, Youyang Sha, Yongjun Yu, Yinzhi Wang, Peizhe Ru, Xuanlong Yu, and Xi Shen. EdgeCrafter: Compact ViTs for edge dense prediction via task-specialized distillation. *arXiv preprint arXiv:2603.18739*, 2026. URL https://arxiv.org/abs/2603.18739.

[19] Juho Lee, Yoonho Lee, Jungtaek Kim, Adam R. Kosiorek, Seungjin Choi, and Yee Whye Teh. Set transformer: A framework for attention-based permutation-invariant neural networks. In *International Conference on Machine Learning (ICML)*, pages 3744–3753, 2019. URL https://arxiv.org/abs/1810.00825.

[20] Han Hu, Jiayuan Gu, Zheng Zhang, Jifeng Dai, and Yichen Wei. Relation networks for object detection. In *IEEE/CVF Conference on Computer Vision and Pattern Recognition (CVPR)*, pages 3588–3597, 2018. URL https://arxiv.org/abs/1711.11575.